



Cite this: *Soft Matter*, 2019,  
15, 5163

Received 27th November 2018,  
Accepted 7th June 2019

DOI: 10.1039/c8sm02397b

rsc.li/soft-matter-journal

## Morphological transitions of axially-driven microfilaments<sup>†</sup>

Yi Man and Eva Kanso \*

The interactions of microtubules with motor proteins are ubiquitous in cellular and sub-cellular processes that involve motility and cargo transport. *In vitro* motility assays have demonstrated that motor-driven microtubules exhibit rich dynamical behaviors from straight to curved configurations. Here, we theoretically investigate the dynamic instabilities of elastic filaments, with free-ends, driven by single follower forces that emulate the action of molecular motors. Using the resistive force theory at low Reynolds number, and a combination of numerical techniques with linear stability analysis, we show the existence of four distinct regimes of filament behavior, including a novel buckled state with locked curvature. These successive instabilities recapitulate the full range of experimentally-observed microtubule behavior, implying that neither structural nor actuation asymmetry are needed to elicit this rich repertoire of motion.

### I. Introduction

Microtubules are one of the main filamentous biopolymers that form the cytoskeleton of eukaryotic cells. They play crucial roles in the structural stability of cells as well as in dynamic processes such as cell motility, division, re-organization, adhesion, and signaling.<sup>1,2</sup> Microtubules are formed of  $\alpha$ - $\beta$  tubulin dimers. The polymerization process by tail-head stacking of these dimers leads to an inherent polarity, with each microtubule characterized by a highly dynamic plus end and a relatively stable minus end.<sup>1,3</sup> Microtubules gain activity through the interactions with motor proteins, namely kinesin and dynein motors. These molecular motors transfer chemical energy in the cytoplasm – in the form of adenosine-triphosphate (ATP) – into mechanical work allowing them to move unidirectionally along microtubules; kinesin motors move towards the plus end, while dynein motors towards the minus end.<sup>1,3</sup> Reciprocally, by the law of action-reaction, molecular motors can exert forces that drive the microtubules into motion.

Microtubules have a persistence length (ratio of elastic to Brownian forces) around 1 mm, which is much larger than their typical length  $L \approx 50 \mu\text{m}$ . Therefore, Brownian forces can be neglected. Individual microtubules can be viewed as elastic rods or filaments, immersed within a fluid, and acted upon by motor proteins.<sup>3,4</sup> Although microtubules constitute a rather stiff part of the cytoskeleton, experiments have found that a microtubule can buckle under the action of a longitudinal force

of magnitude as small as 1 pN.<sup>5</sup> This buckling instability causes the microtubule to deform and assume curved configurations, which have been well observed experimentally in *in vitro* motility or gliding assays. In the gliding assays, molecular motors are attached to a substrate and the microtubules added into the ATP-rich solution are propelled along the surface by the action of the anchored motors.<sup>4–8</sup> Early gliding assays were used to infer the forces exerted by these molecular motors.<sup>4–6</sup> For example, in ref. 9, to estimate the average forces of myosin motors, the authors analyzed the buckling of the actin filaments fixed spatially at their leading end. These actin filaments were shown to undergo both rotations and flapping oscillations and their behavior was analyzed mathematically in the context of elastic beam models.<sup>10</sup> More recently, high-density gliding assays are used as a model system for the collective dynamics of active materials.<sup>7,8</sup> An interesting feature that is consistently observed in these experiments is that, while many microtubules translate in a straight configuration, some microtubules curl into tight arc-shaped configurations and trace circular trajectories or rings with radii of a few tens of microns (see Fig. 1). Meanwhile, other microtubules move on almost regular wavy trajectories, at similar wavelengths and smaller amplitude.<sup>7,11</sup>

Theoretical models that aim at explaining the mechanisms underlying the curling of microtubules in these motility assays attribute it to one of two possibilities: (i) a structural bistability of the tubulin dimers, which allow them to exist in two distinct conformations, one slightly shorter than the other. This causes the microtubule to curve when a portion of its sub-segments switch between the two states, providing a mechanism to create rings *via* an internal change to the microtubule,<sup>12</sup> or (ii) differential binding of molecular motors on opposite sides of the microtubule, which actively contribute to its curling.<sup>13</sup> Although these theories

Department of Aerospace and Mechanical engineering, University of Southern California, CA 90007, USA. E-mail: [Kanso@usc.edu](mailto:Kanso@usc.edu)

† Electronic supplementary information (ESI) available. See DOI: [10.1039/c8sm02397b](https://doi.org/10.1039/c8sm02397b)

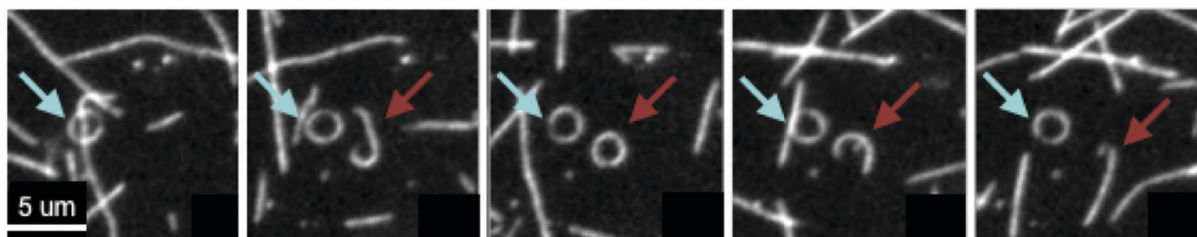


**Fig. 1** Microtubule behavior in motility assays: snapshots extracted from Movie S1 of ref. 7. Many microtubules glide in a straight or wavy configuration. One microtubule (indicated by the green arrow) traces a closed circular trajectory for the full duration of the movie, while another (indicated by the red arrow) enters into a curved state at about 30 s, rotates until about 80 s, then recovers its straight configuration.

are appealing, evidence supporting the hypotheses that structural or actuation asymmetries are required for achieving filament motions at buckled configuration with locked curvature remains circumstantial at best. Here, we propose an alternative, open-loop, mechanism that produces, without inherent asymmetry, the full range of the experimentally-observed microtubule behaviors from straight and undulatory translational motions to circular motions at locked curvatures.

By way of background, it is important to note that the morphological dynamics of active elastic filaments in viscous flows incited a great deal of work in recent years; see, for example ref. 14–17, and references therein for various models of activity profiles. Elastic filaments constitute an excellent model system for understanding various biophysical processes from ciliary beating<sup>18</sup> and flagellar propulsion<sup>19–23</sup> to intracellular streaming.<sup>24</sup> They also form a key ingredient to deciphering the rheological behavior of many complex fluids and soft materials<sup>25,26</sup> and for the collective behavior of active suspensions.<sup>27,28</sup> Here, we present a focused review of this growing literature; the interested reader is referred to ref. 3, 29, 30 and references therein for additional details. De Canio, Lauga and Goldstein recently used a planar filament, anchored at one end and acted upon by a compressive follower force at the distal end to model the action of molecular motors on microtubule filaments.<sup>31</sup> As the force strength increased, the filament underwent a flutter instability leading to planar flapping motions. In ref. 32, the same anchored filament, free to undergo three-dimensional motion, was shown to exhibit richer dynamics, including three-dimensional spinning at a buckled configuration with locked curvature. The role of the hydrodynamic drag can be more significant for a filament with free-ends. Ref. 33 numerically examined the existence of undulatory motions in a model of a free-end filament acted upon by motor forces. The morphological changes of passive actin filaments with free-ends placed in background shear or extensile flows were considered in a series of experimental and theoretical models that showed various transitions from tumbling to coiling and snaking, as discussed in ref. 34 and 35 and references therein.

In this paper, we develop a classic elastohydrodynamic model, balancing elasticity and viscous drag, that takes into account minimal features of the microtubule and motor protein interactions: a free-end elastic filament submerged in viscous fluid and acted upon by a longitudinal point force of constant magnitude

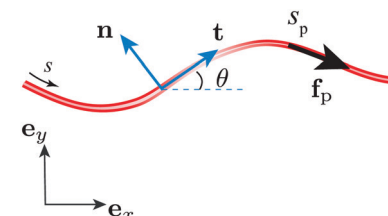


**Fig. 2** Microfilament model: an elastic filament with free ends is driven by a point force  $\mathbf{f}_p$ , located at  $s = s_p$ , where  $s \in [0, L]$  is the arclength from 0 to the total length  $L$ . The local slope is represented by the angle  $\theta$ , and the local tangential and normal directions are  $\mathbf{t}$  and  $\mathbf{n}$ .

that remains tangent to the filament for all time (Fig. 2). We vary the strength and location of the point force along the filament. In the context of this simple model, we observe up to four successive instabilities as we increase the force strength, spanning the full range of experimentally-observed microtubule behavior in the gliding assays. This nonlinear behavior is consistent with a linear stability analysis of the filament dynamics. It is also consistent with a lower-order bead-spring model that clearly gives rise to the structure of the eigenvalues underlying these morphological transitions. In addition, we discuss the role of the location of the actuation force and we present a scaling law that estimates the critical force value where the transition to a locked-curvature occurs.

## II. Microfilament model

We consider a slender elastic filament of length  $L$ , with free ends, actuated by an arbitrary force distribution  $\mathbf{f}_a$  along its centerline. The force  $\mathbf{f}_a(t, s)$  is a function of both time  $t$  and arclength  $s$  along the filament, where  $s \in [0, L]$ . The centerline of the filament is represented by the position vector  $\mathbf{r}(t, s)$  relative a fixed inertial frame  $(\mathbf{e}_1, \mathbf{e}_2, \mathbf{e}_3)$ , where  $(\mathbf{e}_1, \mathbf{e}_2)$  span the plane of motion of the filament. The geometry of the filament can be determined from the local tangential and normal unit vectors  $\mathbf{t}(t, s)$  and  $\mathbf{n}(t, s)$ , chosen such that  $\mathbf{n}$  points in the direction of increasing curvature. Equivalently, the filament geometry can be obtained from the local slope angle  $\theta(t, s)$  of the body frame, such that  $\mathbf{t}_s = \theta_s \mathbf{n}$  and  $\mathbf{t}_t = \theta_t \mathbf{n}$ , where  $\theta_s = \partial \theta / \partial s$  is the curvature of the filament. Here, and throughout this manuscript, we will use the subscript  $(.)_s$  to denote differentiation

with respect to arclength  $s$  and  $\partial_t$  to denote differentiation with respect to time  $t$ .

In addition to the actuation force  $\mathbf{f}_a = f_{\parallel}(t, s)\mathbf{t} + f_{\perp}(t, s)\mathbf{n}$ , the filament is subject to a restoring elastic force  $\mathbf{f}_e$ , that is a function of the filament geometry, and a hydrodynamic drag force  $\mathbf{f}_h$ , which is proportional to the filament velocity. At zero Reynolds number, these forces satisfy the local force balance

$$\mathbf{f}_h + \mathbf{f}_e + \mathbf{f}_a = \mathbf{0}. \quad (1)$$

It is a classical results that the elastic force density  $\mathbf{f}_e$  satisfies<sup>29,36</sup>

$$\mathbf{f}_e = -A\mathbf{r}_{ssss} - [\Lambda(s)\mathbf{r}_s]_s, \quad (2)$$

where  $A$  is the bending rigidity and  $\Lambda$  is the line tension that prevents the filament from being extended or compressed. Mathematically,  $\Lambda$  is a Lagrange multiplier that satisfies the inextensibility constraint  $\mathbf{r}_{ts}\cdot\mathbf{r}_s = 0$ . We calculate the hydrodynamic force  $\mathbf{f}_h$  using the resistive force theory,<sup>37,38</sup> where  $\mathbf{f}_h$  is proportional to the local velocity, with the anisotropic drag coefficients  $\xi_{\perp}$  and  $\xi_{\parallel}$  along the normal and tangential directions respectively,

$$\mathbf{f}_h = -(\xi_{\perp}\mathbf{n}\mathbf{n} + \xi_{\parallel}\mathbf{t}\mathbf{t})\cdot\mathbf{r}_t. \quad (3)$$

Substituting eqn (2) and (3) into eqn (1), we obtain the governing equation as a hyperdiffusive partial differential equation

$$-(\xi_{\perp}\mathbf{n}\mathbf{n} + \xi_{\parallel}\mathbf{t}\mathbf{t})\cdot\mathbf{r}_t - A\mathbf{r}_{ssss} - (\Lambda\mathbf{r}_s)_s + \mathbf{f}_a = \mathbf{0}. \quad (4)$$

We non-dimensionlize eqn (4) by choosing the filament length  $L$  as the length scale and the elastic relaxation time  $\xi_{\perp}L^4/A$  as the time scale; eqn (4) becomes

$$-(\mathbf{n}\mathbf{n} + \gamma\mathbf{t}\mathbf{t})\cdot\mathbf{r}_t - \mathbf{r}_{ssss} - (\Lambda\mathbf{r}_s)_s + \mathbf{f}_a = \mathbf{0}, \quad (5)$$

where  $\gamma = \xi_{\parallel}/\xi_{\perp}$ . Here, we redefined all the variables in dimensionless form, such that tension is scaled by  $A/L^2$ , and force density is scaled by  $A/L^3$ .

We next rewrite eqn (5) in scalar form. To this end, we first take the dot product between eqn (5) and  $\mathbf{t}$ ,  $\mathbf{n}$ , and use the relation  $\mathbf{t}_s = \theta_s\mathbf{n}$ . We arrive at the velocity components

$$\mathbf{r}_t\cdot\mathbf{t} = \gamma^{-1}(3\theta_s\theta_{ss} - \Lambda_s + f_{\parallel}), \quad (6a)$$

$$\mathbf{r}_t\cdot\mathbf{n} = -\theta_{sss} + \theta_s^3 - \Lambda\theta_s + f_{\perp}. \quad (6b)$$

We take the derivative of eqn (6) with respect to  $s$  to obtain

$$\mathbf{r}_{ts}\cdot\mathbf{t} + \theta_s\mathbf{r}_t\cdot\mathbf{n} = \gamma^{-1}[3\theta_{ss}^2 + 3\theta_s\theta_{sss} - \Lambda_{ss} + (f_{\parallel})_s], \quad (7a)$$

$$\mathbf{r}_{ts}\cdot\mathbf{n} - \theta_s\mathbf{r}_t\cdot\mathbf{t} = -\theta_{ssss} + 3\theta_s^2\theta_{ss} - (\Lambda\theta_s)_s + (f_{\perp})_s. \quad (7b)$$

Using the relations  $\mathbf{r}_{ts}\cdot\mathbf{t} = 0$  and  $\mathbf{r}_{ts}\cdot\mathbf{n} = \theta_t$  and eqn (6), we obtain the scalar form of the governing equations for  $\theta(t, s)$  and  $\Lambda(t, s)$ , namely,

$$\begin{aligned} \theta_t &= -\theta_{ssss} - \Lambda\theta_{ss} - (1 + \gamma^{-1})\Lambda_s\theta_s \\ &\quad + 3(1 + \gamma^{-1})\theta_s^2\theta_{ss} + \gamma^{-1}f_{\parallel}\theta_s + (f_{\perp})_s, \end{aligned} \quad (8a)$$

$$\begin{aligned} \Lambda_{ss} - \gamma\theta_s^2\Lambda &= 3\theta_{ss}^2 + (3 + \gamma)\theta_{ss}\theta_{sss} \\ &\quad - \gamma\theta_s^4 + (f_{\parallel})_s - \gamma f_{\perp}\theta_s. \end{aligned} \quad (8b)$$

The boundary conditions for the filament with free-ends are given by the moment- and force-free conditions  $\mathbf{r}_{ss} = 0$  and  $\mathbf{r}_{sss} = 0$  at both ends  $s = 0$  and  $s = L$ , leading to

$$\theta_s(0) = \theta_{ss}(0) = \theta_s(1) = \theta_{ss}(1) = 0, \quad (9a)$$

$$\Lambda(0) = \Lambda(1) = 0. \quad (9b)$$

In obtaining eqn (8) from eqn (6),  $\theta$  and  $\Lambda$  got decoupled from the translational motion of the filament. This decoupling, or reduction, is possible because the filament dynamics is invariant under rigid body translations. To obtain the full filament dynamics, we first solve for the filament geometry  $\theta$  (shape and orientation) and tension  $\Lambda$  using eqn (8), together with the boundary conditions in eqn (9), then we calculate the translational velocity using eqn (6) and solve for the translational motion of the filament.

We consider the case where the filament is pushed by a single follower force exerted at the point  $s = s_p$ ,  $s_p \in (0, 1)$ , such that  $f_{\perp} = 0$  and  $f_{\parallel}(s) = f_p\delta(s - s_p)$ , where  $f_p$  is constant, and the actuation force profile is given by

$$\mathbf{f}_a = f_p\delta(s - s_p)\mathbf{t}. \quad (10)$$

We numerically solve eqn (8) and (9). To smooth the singularity, we use the regularized form of the Dirac delta function

$$\delta_{\varepsilon}(x) \approx \frac{1}{\sqrt{2\pi\varepsilon}}e^{-\frac{x^2}{2\varepsilon^2}}, \quad (11)$$

where  $\varepsilon$  is a small regularization parameter. Details of the numerical methods can be found in the ESI.<sup>†</sup><sup>39</sup>

### III. Linearized equations

For actuation forces  $\mathbf{f}_a = f_p\delta(s - s_p)\mathbf{t}$  of constant magnitude  $f_p$ , the straight filament configuration is a relative equilibrium of eqn (8). That is to say, starting from a straight configuration, the filament remains straight for all time and translates freely along its tangential direction, at a constant translational velocity dictated by the balance between the applied force  $\mathbf{f}_a$  and the hydrodynamic drag force  $\mathbf{f}_h$ .

To investigate the stability of these relative equilibria, we assume small filament deformations and linearize eqn (8) about the straight configuration to get

$$\theta_t = -\theta_{ssss} - \Lambda\theta_{ss} - (1 + \gamma^{-1})\Lambda_s\theta_s + \gamma^{-1}\theta_s f_p(s - s_p), \quad (12a)$$

$$\Lambda_{ss} = f_p[\delta(s - s_p)]_s. \quad (12b)$$

We integrate eqn (12b), together with the boundary conditions in eqn (9b), to obtain an expression for the tension  $\Lambda$  along the filament,

$$\Lambda(s) = f_p[H(s - s_p) - s], \quad (13)$$

where  $H(s - s_p)$  is the Heaviside step function. Then, we substitute eqn (13) into eqn (12a) to get the linear equation for  $\theta$

$$\theta_t = -\theta_{sss} - f_p[H(s - s_p) - s]\theta_{ss} - f_p[\delta(s - s_p) - (1 + \gamma^{-1})]\theta_s. \quad (14)$$

To solve this linear partial differential equation, we assume separation of time and space such that

$$\theta(s, t) = \hat{\theta}(s)e^{\omega t}, \quad (15)$$

with the initial condition  $\theta(s, t = 0) = \hat{\theta}(s)$  and growth rate  $\omega$ . We substitute eqn (15) into eqn (14) to obtain, together with the free-ends boundary conditions (9a) for  $\hat{\theta}$ , the eigenvalue problem

$$\begin{aligned} \omega\hat{\theta} = & -\hat{\theta}_{sss} - f_p[H(s - s_p) - s]\hat{\theta}_{ss} \\ & - f_p[\delta(s - s_p) - (1 + \gamma^{-1})]\hat{\theta}_s. \end{aligned} \quad (16)$$

This eigenvalue problem is not trivial to solve due to the appearance of non-constant coefficients in the linear ordinary differential equation. Here, we compute the eigenvalues numerically by discretizing the right-hand of eqn (16) using a second-order, finite-difference approximation.

## IV. Microfilament behavior

We numerically investigate the behavior of the elastic filament under an axial point force  $f_p L^3/A$  applied at  $s_p/L = 0.4$ . Here, we use the dimensional form of  $s_p$  and  $f_p$ . Starting from a slightly-curved initial geometry, we systematically increase the value of the dimensionless force magnitude  $f_p L^3/A$  such that  $f_p L^3/A = 80, 180, 220, 290$ , and  $300$ . We observe five successive regimes of motion and filament configuration, from straight to oscillatory motions. Fig. 3 depicts the corresponding trajectories in a fixed inertial frame. In Fig. 3(a), at relatively small magnitude  $f_p L^3/A = 80$ , the filament relaxes uniformly to its straight shape while it translates along a fixed direction determined by initial conditions. At  $f_p L^3/A = 180$ , the filament buckles into a curved shape as it translates and rotates rigidly while maintaining a locked-curvature as shown in Fig. 3(b); the radius of the circular trajectory traced by the filament depends on  $f_p L^3/A$  but is independent of initial conditions. Specifically, this radius first decreases as  $f_p L^3/A$  increases, reaches a minimum, then increases again. In Fig. 3(c), as we increase the force further to  $f_p L^3/A$ , a counter-intuitive motion occurs where the filament escapes from the circular motion and relaxes back to the straight shape. This ‘escape’ behavior is observed for a relatively short range of forces. For larger values of  $f_p L^3/A$ , the filament oscillates while undergoing a translational motion. At first, the oscillation amplitude decays to zero as shown in Fig. 3(d) for

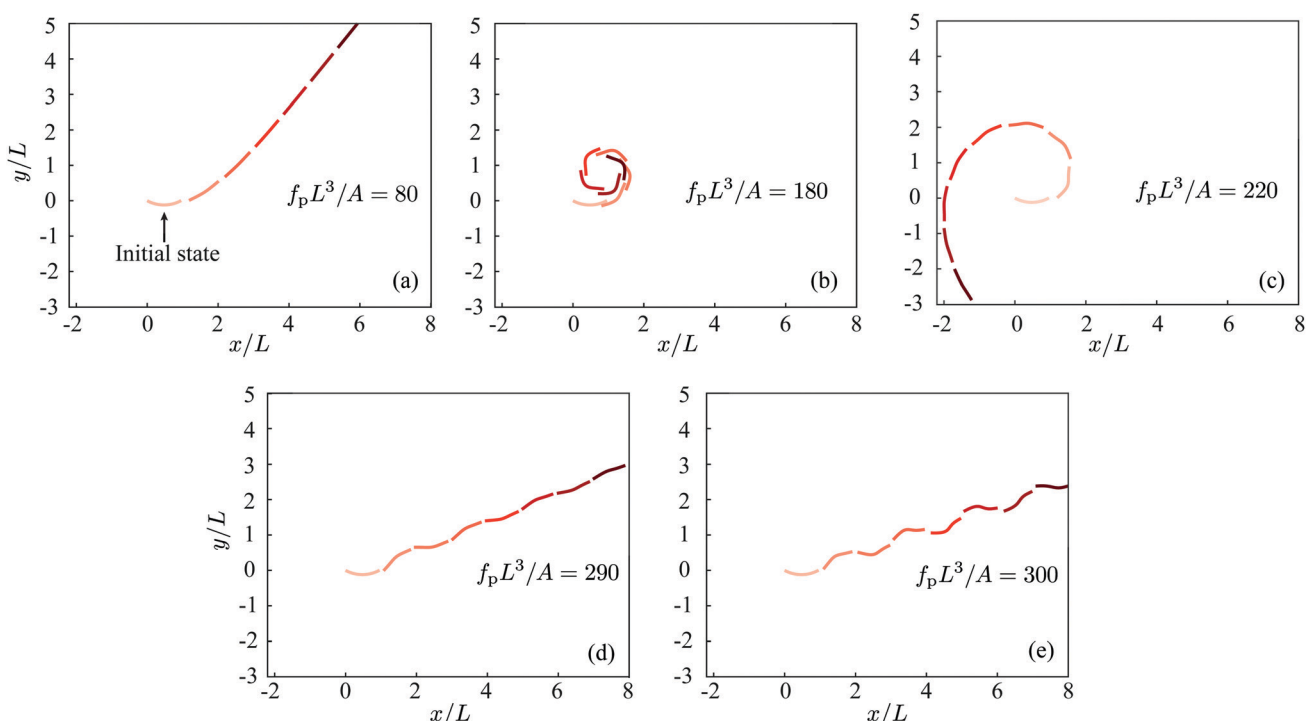


**Fig. 3** Trajectory of the filament actuated by a tangential point force applied at  $s_p/L = 0.4$ , with dimensionless force magnitude  $f_p L^3/A$ . The initial state is a curved geometry, shown in faded color. Darker color corresponds to increasing time. (a) For  $f_p L^3/A = 80$ , the filament recovers its straight geometry. (b) Increasing the force to  $f_p L^3/A = 180$ , the filament undergoes a circular motion with a locked curvature. (c) However, at a larger force  $f_p L^3/A = 220$ , the filament escapes from the circular motion and recovers its straight geometry again. (d) At  $f_p L^3/A = 290$ , the filament exhibits decaying oscillations as it returns to its straight shape. (e) At  $f_p L^3/A = 300$ , the amplitude grows to a bounded value and the filament demonstrates a motion similar to undulatory swimming (see Movies S1–S5, ESI†).

$f_p L^3/A = 290$ . At larger force values, the filament undergoes sustained oscillations, at bounded amplitudes, similar to those observed in undulatory swimming, as shown in Fig. 3(e) for  $f_p L^3/A = 300$ .

We calculate the dimensionless bending energy  $2E_b L/A$ ,

$$\frac{2E_b L}{A} = \int_0^1 \theta_s^2 ds', \quad (17)$$

associated with each of these regimes. In Fig. 4, we plot the bending energy *versus* time for the five cases shown in Fig. 3; the insets represent the filament geometry in a body frame fixed at  $s_p/L = 0.4$ . The initial geometry is highlighted in a faded (red) color and later geometries are shown in deeper color as time evolves. Clearly, the bending energy goes to zero when the filament returns to its straight configuration in Fig. 4(a, c and d), with the exception that in the latter, the decaying oscillations of the filament are manifested in decaying oscillations of the corresponding bending energy. In Fig. 4(b), the bending energy reaches a nonzero constant, corresponding to the internal energy stored in the filament at this locked-curvature whereas in Fig. 4(e) the bending energy oscillates in time. Note that even if the applied force increases from  $f_p L^3/A = 180$  in (b) to  $f_p L^3/A = 300$  in (e), the bending energy decreases. This corresponds to the increase in hydrodynamic dissipations with the filament oscillation comparing to the locked-curvature motion.

In Fig. 5(a), we systematically examine the long-term nonlinear behavior of the filament by plotting the corresponding bending energy as a function of the applied force. As  $f_p L^3/A$  increases from 0 to 300, we observe successive changes in the stored elastic energy that reflect the distinct regimes of filament behavior from straight (1) to curved with locked shape (2), back to straight (1), then to decaying oscillations (3), and finally to bounded oscillations (4). In the latter, we report the maximum, minimum, and average values of the elastic energy, as highlighted in the grey region in Fig. 5(a). The transitions between these regimes occur at around  $f_p L^3/A = 111, 213, 234$  and 297. It is worth noting that in regime (2), as  $f_p L^3/A$  increases, the filament curvature increases (implied from the bending energy in Fig. 5(a)), reaches a maximum, then decreases, in a way that is inversely proportional to the radius of the circular trajectory traced by the filament (Fig. 3b). Specifically, as the filament curvature decreases, the radius increases until the filament ‘escapes’ from this regime and returns to a stable straight configuration.

## V. Linear stability analysis

We next analyze the linear stability of the filament subject to small deformations by computing the eigenvalues  $\omega$  associated with eqn (16). In Fig. 5(b), we report the real and imaginary components of the dominant branch, the branch with the

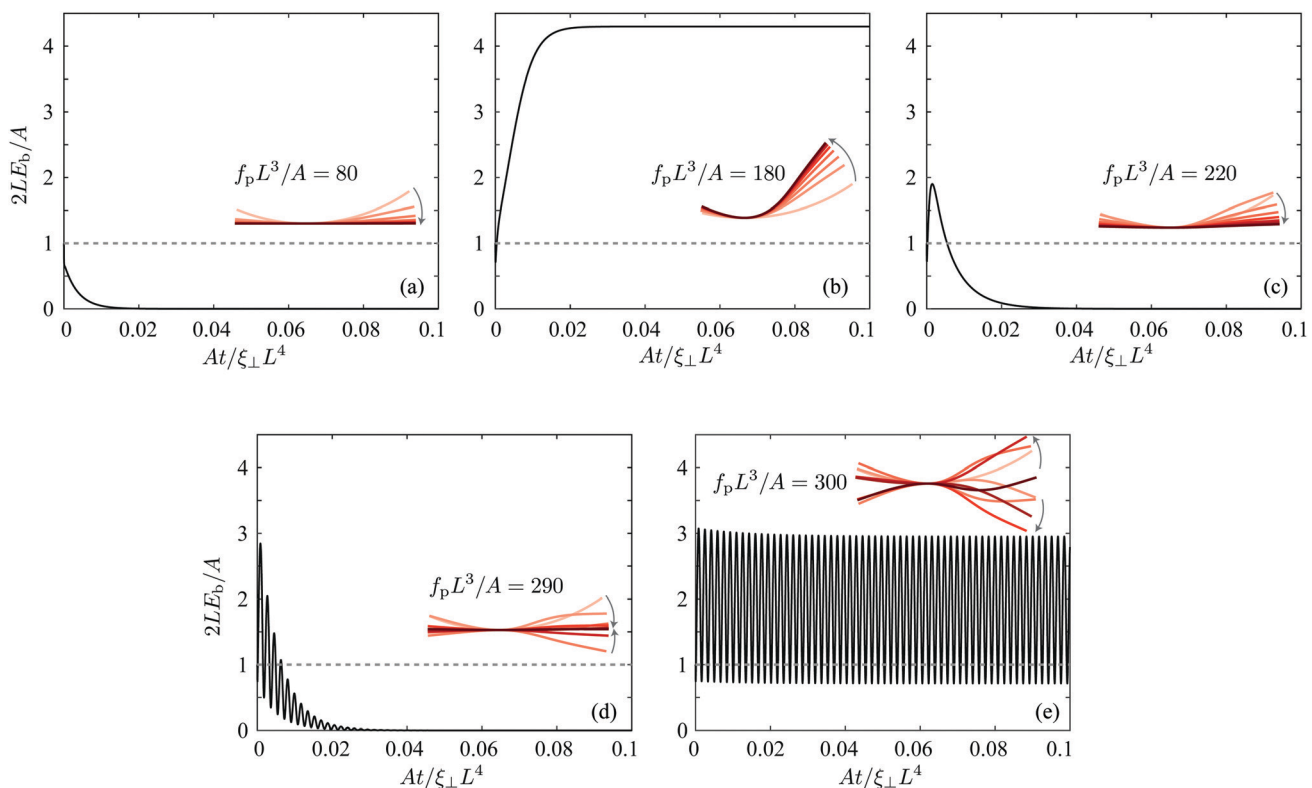


**Fig. 4** Bending energy of the filament as a function of time for the trajectories shown in Fig. 3. The inset figures depict the changes in the filament geometry in the body frame fixed at  $s_p$ ; darker colors correspond to increasing time. The dashed line of  $2LE_b/A = 1$  is the bending energy of the initial configuration.

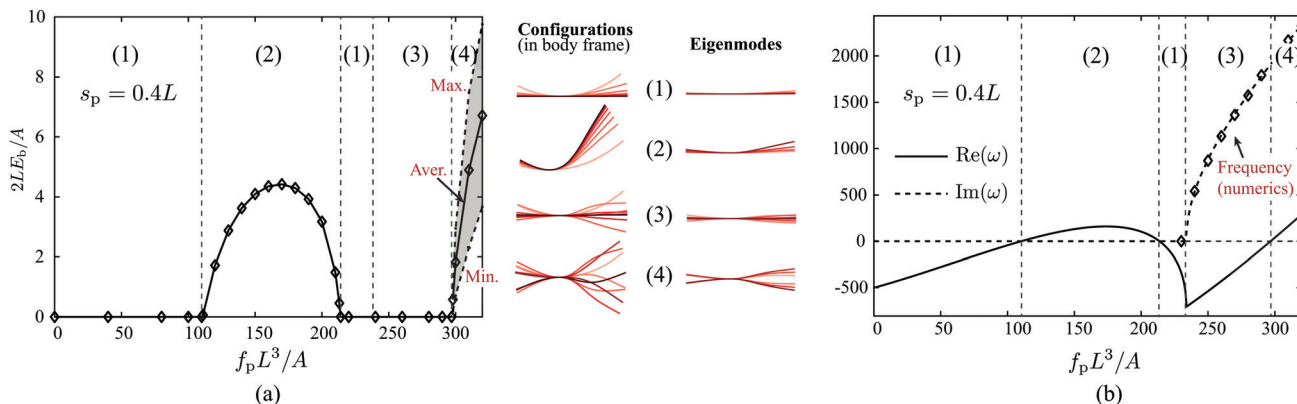


**Fig. 5** (a) Bending energy of the steady states as a function of the applied force in the case  $s_p = 0.4$ . As  $f_p L^3/A$  increases from 0 to 300, we observe successive changes in the stored elastic energy that reflect the distinct regimes of filament behavior from straight (1) to a buckled state with locked shape (2), back to straight (1), to decaying oscillations (3), and finally to bounded oscillations (4). Filament configurations in the body frame are shown to the right. In regime (4), we report the maximum, minimum, and average values of the elastic energy, as highlighted in the grey region. The transitions between these regimes occur at around  $f_p L^3/A = 111, 213, 234$  and  $297$ . (b) The dominant branch of the eigenvalue  $\omega$  as a function of the applied force, the real component is plotted in solid line, while the imaginary part is plotted in dashed line. In regime (4), we superimpose the oscillation frequencies (shown as diamond markers) obtained from the nonlinear simulations. The results of the linear stability analysis are consistent with the nonlinear analysis in (a). In addition, the configurations of the eigenmodes associated with the dominant branch  $\hat{\theta}(s)e^{\omega t}$  are shown to the left.

largest nonzero real part  $\text{Re}(\omega)$ , as a function of  $f_p L^3/A$ . Note that we ignore the trivial branch ( $\omega = 0$ ) associated with the translational symmetry of the filament. As in Fig. 5(a), the linear stability analysis shows five regimes, the first and third are stable, with  $\omega$  real and negative, while the second is unstable, with  $\omega$  real and positive, indicating that the straight filament configuration is unstable. The imaginary part of  $\omega$  becomes nonzero when the force for  $f_p L^3/A \geq 234$  with negative real part at first, indicating decaying oscillations but as  $f_p L^3/A$  increases past 300, the real part  $\text{Re}(\omega)$  becomes positive indicating linearly growing oscillations and unstable straight configuration. On the left of Fig. 5(a), we plot the eigenmodes associated with the dominant branch  $\hat{\theta}(s)e^{\omega t}$ ; darker color indicates increasing time. The oscillation frequencies obtained from the nonlinear simulations in regime (4) are shown as diamond markers in Fig. 5(b), indicating perfect agreement with the frequencies  $\text{Im}(\omega)$  obtained from the linear stability analysis.

We compare the filament behavior to the two limit cases where the force is applied at one of the filament's ends, either pushing the filament ahead for  $s_p = 0$  or pulling it behind for  $s_p/L = 1$ . The eigenvalues of these limit cases are plotted in Fig. 6. For  $s_p = 0$ , the filament transitions from stable to oscillatory motion, but it does not exhibit a buckled state with locked curvature. For  $s_p/L = 1$ , the straight configuration is always stable due to the extensile stress everywhere in the filament. It is worthwhile to mention that the limit  $s_p/L \rightarrow 1$  is a singular limit. In this limit, an infinitesimal portion ( $s_p/L, 1]$ ) of the filament is always under compression due to the applied force; thus the filament can, in theory, buckle, albeit at very large forces. At  $s_p/L = 1$ , the filament is in pure tension and buckling is not possible.

To quantify the role of the location of the applied force on the filament behavior, we vary both the location  $s_p/L$  and magnitude  $f_p L^3/A$  of the applied force and classify the filament's

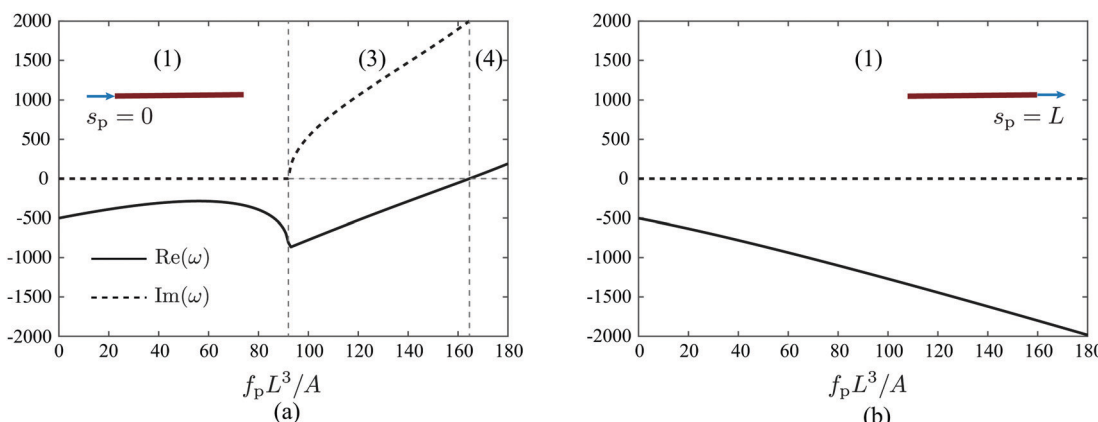


**Fig. 6** Eigenvalues of the two limit cases: (a) pushing force at  $s_p = 0$ ; (b) pulling force at  $s_p = 1$ . In (a), only three regimes of motion are observed: stable, decaying oscillations and growing oscillations. In (b), the filament is always stable, which can be proved as a singular limit.

behavior according to the eigenvalues of the linear stability analysis. For each value of  $s_p/L$ , we compute the values of the critical force that marks the transitions in the filament behavior. We map the filament behavior onto the phase space  $(s_p/L, f_p L^3/A)$  in Fig. 7, which shows four regions with four distinct filament behaviors: stable, buckled with locked curvature, decaying oscillations and sustained oscillations. The buckled behavior with locked curvature occurs in an “island” that appears only for  $0.35 < s_p/L < 1$  when the force is applied away from the two ends of the filaments.

To elucidate the physical mechanisms at play in these regimes, we note that the filament can be split into two segments: the segment trailing the location of the applied force is under tension while the segment ahead is under compression. The interplay between these two segments allows the filament, for a range of values of the applied forces, to buckle into a curved configuration with locked-curvature. A simple scaling argument suggests that, in addition to the elastic relaxation time scale  $T_e \sim \zeta L^4/A$  that we used as a characteristic time to obtain the non-dimensional form of the equations of motion, there are two additional time scales associated with the portion of the filament under compression: a time scale  $T_p \sim \zeta(L - s_p)/f_p$  that arises from balancing the applied force with the hydrodynamic drag on a straight filament in translational motion, and a time scale  $T_c \sim \zeta(L - s_p)^4/A$  that is obtained by balancing drag with the elastic force. If  $s_p/L = 1$ , the time scale  $T_c = 0$  implying that the elastic forces required to deform the filament are infinitely large; the filament does not deform, consistent with the linear stability analysis in Fig. 6. When  $s_p = 0$ , the two time scales  $T_c$  and  $T_e$  are identical. The ratio  $T_e/T_p$  is equal to the dimensionless force  $f_p L^3/A$ . For large force values ( $T_e/T_p \gg 1$ ), the translational motion happens much faster than the elastic deformation; the filament has no time to relax, instead it buckles. For  $0 < s_p < L$ , the ratio  $T_c/T_p$  is

equal to  $(f_p L^3/A)((L - s_p)^3/L^3)$ . The condition  $T_c/T_p \sim 1$  implies a buckling criterion  $f_p L^3/A \sim L^3/(L - s_p)^3$ . This buckling criterion is superimposed onto in the phase space in Fig. 7. For  $s_p/L > 0.35$ , this simple scaling argument shows excellent agreement with the transition from stable to buckled state.

In practice, multiple molecular motors can simultaneously bind to the same microtubule, generating a distribution of forces along the microtubule length. It is therefore worthwhile to investigate the influence of multiple point forces and of continuous force distributions on the filament behavior. To this end, we consider the following two scenarios: (i) a filament subject to two point forces  $f_1 = f_2 = f_p$  located at  $s_1$  and  $s_2$ , respectively, and (ii) a filament subject to a Gaussian force density as in (6) and (7), with a standard deviation  $\varepsilon$  that is not necessarily small. To compare the behavior of the filament under these force profiles to its behavior under a single force, we fix one force at  $s_1 = 0.4$  as done in Fig. 3–5. In Fig. 8(a), we vary the position  $s_2$  of the second force and in Fig. 8(b), we vary  $\varepsilon$ . The dominant eigenvalue, with real part shown in solid lines and imaginary part shown in dashed lines, is shown in Fig. 8(a) for three cases: (I)  $s_2 = 0.2$ , (II)  $s_2 = 0.5$ , and (III)  $s_2 = 0.8$ , force profiles are all depicted to the right. For  $s_2 = 0.2$ , the filament transitions from straight to first decaying, then sustained, oscillations as the force strength increases. For  $s_2 = 0.5$ , the filament exhibits a buckled state at locked curvature for a range of force values similar to that reported in the case of a single force. For  $s_2 = 0.8$ , the straight configuration is stable and transitions to oscillatory motions occur at much larger values of the force. These results show that there exists a range of separation distances between pairs of forces of equal strength for which the filament exhibits all the behaviors reported in Fig. 7 for a single force. Also by continuity, we expect the filament to exhibit similar behaviors for a range of force values when the two forces are not of equal strength. Fig. 8(b) depicts the dominant eigenvalue for a Gaussian force profile for (I)  $\varepsilon = 0.01$ , (II)  $\varepsilon = 0.05$ , and (III)  $\varepsilon = 0.1$ . The buckled state at locked-curvature is observed for  $\varepsilon = 0.01$  and  $\varepsilon = 0.05$ , and disappears for  $\varepsilon = 0.1$  as the force profile flattens. This is in contrast to the results in ref. 14, where spiral deformations are observed for tangential forces that are uniformly applied along the filament. We attribute this distinction in behavior to fundamental differences in the filament model. In ref. 14, the filament is composed of a chain of colloidal particles that experience internal bond forces and excluded-volume repulsion forces in addition to bending resistance that differs from the bending model considered here.

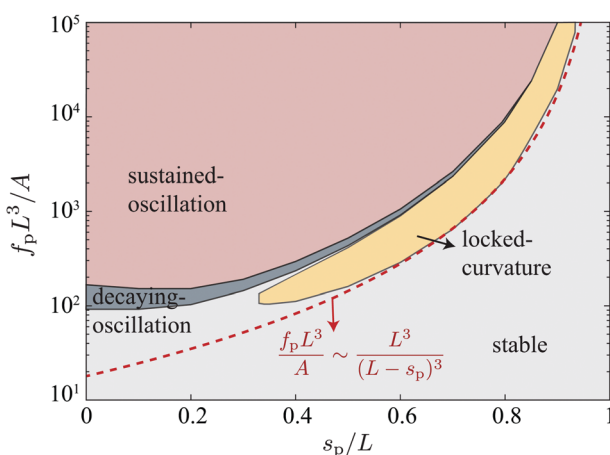
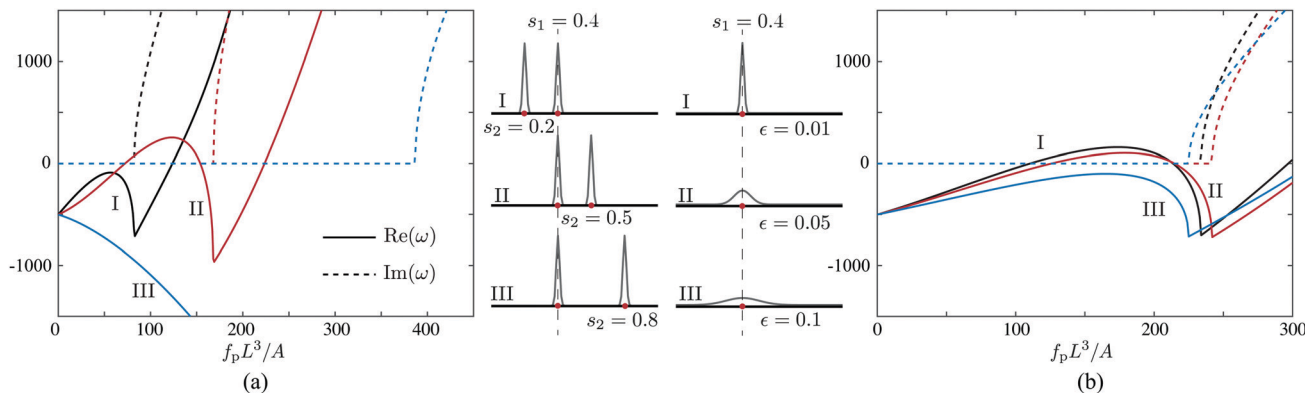


Fig. 7 Phase space of the filament behavior as a function of  $(s_p/L, f_p L^3/A)$ , plotted on a semi-log scale. Four distinct filament behaviors are observed: stable (straight filament undergoing translational motion), buckled state with locked curvature (curved filament tracing a circular trajectory), stable with decaying oscillations, and buckled state with sustained oscillations (filament oscillates while undergoing translational motion reminiscent to undulatory swimming). The dashed line indicates the approximate scaling law of the critical value that buckling occurs.

## VI. Spring-bead model

Our goal in this section is to gain more insight into the appearance of the locked-curvature state (the yellow region in Fig. 7), and the transition from this to oscillatory motions. In particular, we would like to confirm that the mechanism leading for this locked-curvature state depends on the interplay between the two portions of the filament: the trailing portion that is under tension and the portion ahead of the axial force that is under compression. To this end, we consider a bead-spring



**Fig. 8** Linear stability analysis: (a) filament subject to two point forces of equal strength as shown to the right; one force is fixed at  $s_1 = 0.4$  and the second force is located at  $s_2 = 0.2$  (black), 0.5 (red), and 0.8 (blue), and (b) filament subject to a Gaussian force profile with standard deviations  $\epsilon = 0.01$  (black), 0.05 (red), and 0.1 (blue) as shown to the left. The eigenvalues are calculated with respect to the force magnitude, the real parts of the dominant eigenvalue are represented in solid lines, and the imaginary parts in dashed lines.

model with the aim of reproducing these effects with the minimum number of degrees of freedom. Specifically, we study a simpler model consisting of a chain of  $N + 1$  spherical beads linked by  $N$  rigid rods, with a torsional spring of constant rotational stiffness coefficient  $k$  at each joint. The total length of the chain is  $L$ . The position of each bead is denoted by  $\mathbf{r}_i$ , with  $i = 0, \dots, N$ , and satisfies  $\mathbf{r}_{i+1} = \mathbf{r}_i + L/N\mathbf{t}_i$ , where  $\mathbf{t}_i$  is a unit vector representing the orientation of the  $i$ th link, where  $i$  changes from 1 to  $N$ . The chain is subject to an external force  $\mathbf{F}$  applied at one joint, say joint  $p$ , parallel to the link connecting joint  $p$  to joint  $p + 1$  such that  $\mathbf{F} = F\mathbf{t}_p$ , where  $p$  is the index of the chosen link. As  $p$  increases, with all other parameters held constant, the portion of the chain that is being pulled increases while the portion that is being pushed or compressed decreases. On the other hand, as  $N$  increases, keeping all other parameters the same, the opposite is true: the pulled portion of the chain decreases and the pushed portion increases. By comparing the behavior of the chain for various  $N$  and  $p$ , we can confirm that the interplay between these two segments is a universal mechanism that governs the transitions between various behaviors. Specifically, we expect a transition to oscillatory motion as  $N$  increases and a gradual inhibition of these buckling instabilities as  $p$  increases.

It is convenient for what follows to scale all lengths by the total length  $L$  of the chain. Considering a net drag coefficient  $\xi$  on the chain, we scale time by  $\xi L^2/k$ . The force  $F$  is then scaled by  $k/L$ . The scaled drag coefficient on each bead is  $1/(N+1)$ . We write the equations of motion of the chain in dimensionless form. First, the force balance on the whole chain leads to

$$F\mathbf{t}_p - \frac{1}{N+1} \sum_{i=0}^N \mathbf{v}_i = 0, \quad (18)$$

where  $\mathbf{v}_i = \mathbf{r}_{it}$  denotes the velocity of the  $i$ th bead. Then, on the  $j$ th link, the moment about  $\mathbf{r}_{j-1}$  is balanced in terms of the inner forces and the torsional springs. Namely, for  $j < p$ , one has

$$\mathbf{n}_j \cdot \left( F\mathbf{t}_p - \frac{1}{N+1} \sum_{i=j}^N \mathbf{v}_i \right) - \Theta_{j-1} + \Theta_j = 0, \quad (19)$$

whereas, for  $j \geq p$ ,

$$-\frac{1}{N(N+1)} \mathbf{n}_j \cdot \sum_{i=j}^N \mathbf{v}_i - \Theta_{j-1} + \Theta_j = 0. \quad (20)$$

Here, we defined  $\Theta_j = \theta_{j+1} - \theta_j$ , for  $j = 1, 2, \dots, N-1$ , to represent the relative angles between two consecutive links. This definition is ambiguous at the two free ends of the chain; to disambiguate, we define  $\Theta_0 = \Theta_N = 0$ .

By construction,  $\mathbf{v}_{i+1} = \mathbf{v}_i + \theta_{it}\mathbf{n}_i/N$ , which we substitute into eqn (18) to calculate  $\mathbf{v}_0$ ,

$$\mathbf{v}_0 = F\mathbf{t}_p - \frac{1}{N(N+1)} \sum_{i=1}^N (N-i+1)\theta_{it}\mathbf{n}_i. \quad (21)$$

We also use  $\mathbf{v}_{i+1} = \mathbf{v}_i + \theta_{it}\mathbf{n}_i/N$  to obtain an expression for  $\mathbf{n}_j \cdot \sum_{i=j}^N \mathbf{v}_i$ , namely,

$$\begin{aligned} \mathbf{n}_j \cdot \sum_{i=j}^N \mathbf{v}_i &= (N-j+1)F \sin(\theta_p - \theta_j) \\ &+ \frac{1}{N(N+1)} \sum_{i=1}^j i(N-j+1)\theta_{it} \cos(\theta_i - \theta_j) \\ &+ \frac{1}{N(N+1)} \sum_{i=j+1}^N j(N-i+1)\theta_{it} \cos(\theta_i - \theta_j). \end{aligned} \quad (22)$$

We substitute eqn (22) into eqn (19) and (20) to get a closed system of  $N$  nonlinear ordinary differential equations for the  $N$  degrees of freedom  $\theta_j, j = 1, 2, \dots, N$ , that describe the shape and orientation of the chain. We solve this system numerically to obtain the deformation and rotational motion of the spring-bead chain.

Similar to the full filament model, the straight configuration of the chain is a relative equilibrium of the nonlinear equations of motion. To analyze the stability of this relative equilibrium, we assume small deformations and linearize the equations of

motion for  $\theta_j$ . We get that, for  $j < p$ ,

$$\begin{aligned} \sum_{i=1}^j i(N-j+1)\theta_{it} + \sum_{i=j+1}^N j(N-i+1)\theta_{it} \\ = N^2(N+1)^2 \left[ \frac{j}{N(N+1)} F(\theta_p - \theta_j) - \Theta_{j-1} + \Theta_j \right], \end{aligned} \quad (23)$$

and, for  $j \geq p$ ,

$$\begin{aligned} \sum_{i=1}^j i(N-j+1)\theta_{it} + \sum_{i=j+1}^N j(N-i+1)\theta_{it} \\ = N^2(N+1)^2 \left[ -\frac{(N-j+1)}{N(N+1)} F(\theta_p - \theta_j) - \Theta_{j-1} + \Theta_j \right]. \end{aligned} \quad (24)$$

We first consider a minimal case of two links. When the force is exerted on the first link ( $p = 1$ ), an instability occurs at  $FL/k = 12$ . For example, in Fig. 9(a), we solve the nonlinear equations eqn (18)–(20) for  $FL/k = 13$  and with an initial condition slightly-perturbed from the straight configuration. The links fold into a “V” shape at a locked angle  $\Theta_1 = \Delta\theta = \theta_2 - \theta_1$ , and undergo a circular motion reminiscent to that observed in Fig. 3(b). The angle  $\Delta\theta$  can be calculated analytically from the nonlinear equations by assuming a rigid-body motion of the links, with rotation rate  $\Omega = \dot{\theta}_{1t} = \dot{\theta}_{2t}$ . We get that  $FL/k = 12\Delta\theta/\sin\Delta\theta$ . This yields  $\Delta\theta \approx 0.69$  for  $FL/k = 13$ , which matches the numerical results shown in Fig. 9(a). The instability can be tested by solving the linearized equations eqn (23) and (24), which gives rise to one nonzero eigenvalue  $\omega_1 = 6(FL/k - 12)$ , depicted in Fig. 9(b), and confirming the nonlinear analysis that for  $FL/k > 12$ , the straight configuration of the two-link chain becomes unstable.

In an effort to capture the transition from a buckling at a locked shape to oscillatory motions, we increase the number of links while applying the force at  $p = 1$ . We observe the following sequence of bifurcations in the chain behavior. When  $N = 3$ , we obtain two nonzero eigenvalues  $\omega_1 = 6(FL/k - 12)$  and  $\omega_2 = 18(FL/k - 20)$ , implying that the three-link chain becomes unstable for  $FL/k > 12$ , but cannot exhibit oscillatory motions. For  $N = 4$ , we obtain three nonzero eigenvalues, including two branches with nonzero imaginary part, indicating oscillatory motions. In Fig. 9(c), we show an example of such oscillations by solving the nonlinear equation for  $FL/k = 23$ . In Fig. 9(d), we show the three branches of the eigenvalues as a function of the applied force  $FL/k$ ; the non-positive real eigenvalues  $\omega_1$  and  $\omega_2$  collide at  $FL/k = 15.3$  to give rise a complex pair, first with a negative real part (decaying oscillations), then positive real part at  $FL/k = 16.6$  (growing oscillations). The dominant branch shown in the inset of Fig. 9(d) resembles the dominant branch in Fig. 6(a). Thus, at  $p = 1$  and  $N = 4$ , the structure of the eigenvalue problem does not lead to a transition from the locked shape to oscillatory deformations. This is true for all  $N$  when  $p = 1$ , as evidenced in Fig. 10(a). The phase space in Fig. 10(a) depicts the chain behavior as a function of the length of each link (the inverse  $1/N$  of the number of links) and applied force  $FL/k$ . As  $N \rightarrow \infty$ , the chain model approaches

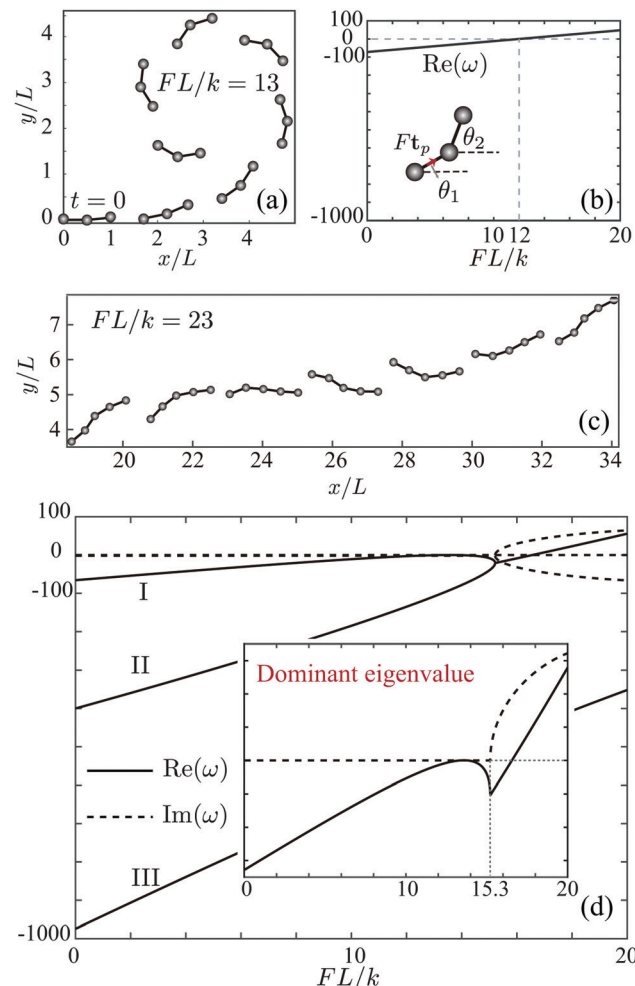
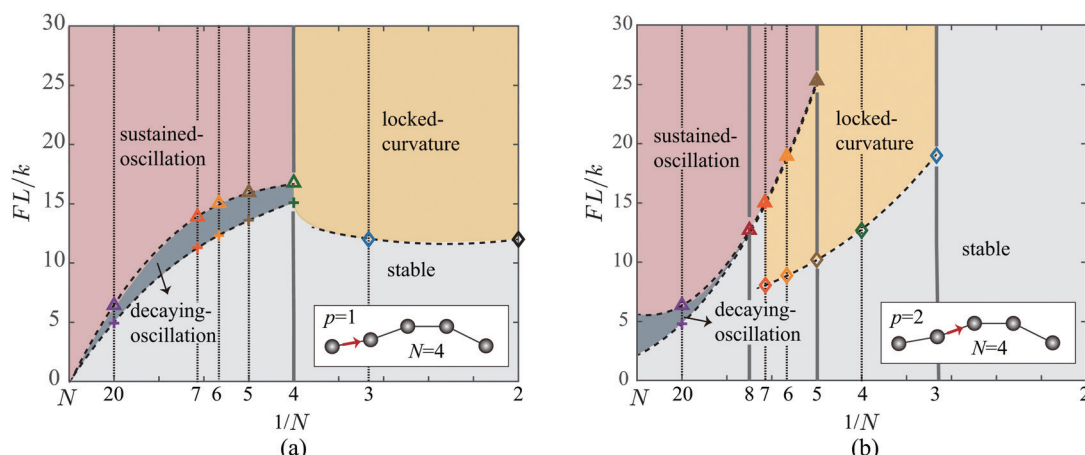


Fig. 9 Spring-bead model: (a) for  $N = 2$ ,  $p = 1$ , the chain undergoes a circular motion at a locked shape when  $FL/k > 12$ . (b) at  $FL/k > 12$ , the only nonzero eigenvalue  $\omega_1$  obtained the linear stability analysis becomes positive. (c) For  $N = 4$ ,  $p = 1$ , the chain undergoes oscillatory motion for  $FL/k = 23$ . (d) Linear stability analysis reveals three eigenvalues, that are all real for small  $FL/k = 23$ . The real parts are plotted with solid lines, and the imaginary parts with dashed lines; the inset shows the dominant eigenvalue. The two branches  $\omega_{1,2}$  collide at  $FL/k = 15.3$ , forming a Hopf bifurcation reminiscent of the dominant branch of the continuous filament in Fig. 6(a).

the full filament model, with force applied near the proximal end of the filament.

When the force is exerted on the second link ( $p = 2$ ), the straight configuration is unconditionally stable for  $N = 2$ , when the chain is being mostly pulled by the applied force, and exhibits a transition to a locked-curvature state for  $N = 3$  and  $N = 4$ . For these  $N$  values, the dominant eigenvalue is similar to that shown in Fig. 9(d) (results not shown for brevity), and thus transitions to oscillatory motions are not permitted. However, at  $N = 5$ , the chain exhibits two successive instabilities as  $FL/k$  increases, first from straight to a shape with locked curvature, then to sustained oscillations as shown in Fig. 10(b).

In summary, when the force is applied to the first link (Fig. 10(a)), as we vary the total number of links and the



**Fig. 10** The phase space summarizing the behavior of the bead-spring model as a function of  $(1/N, FL/k)$ . Results are constructed based on linear stability analysis and confirmed using numerical simulations of the nonlinear equations. (a) for  $p = 1$ , the force  $FL/k$  is applied on the first link. At  $N \geq 4$ , the chain transitions from straight to oscillatory motions and the buckled regime with locked-curvature disappears; (b) for  $p = 2$ , the force  $FL/k$  is applied at the second link. With one trailing link, we observe a transition from locked-curvature to oscillations when  $N \geq 5$ .

magnitude of the applied force, the chain exhibits a transition to circular trajectories at locked shape for  $N \leq 3$  and to oscillatory motions for  $N \geq 4$ , and no transition between these two states for any  $N$ . In contrast, when the force is applied to the second link (Fig. 10(b)), allowing for a greater portion of the chain to trail behind the applied force, we recover the transitions from straight to curved shape, then from curved shape to oscillatory motions for  $5 \leq N \leq 7$ . Taken together, these results indicate that the transition from locked curvature to oscillatory motion requires (i) a minimum number of degrees of freedom in the portion of the chain that is under compression, and (ii) a sufficient portion of the chain should be trailing behind the location of the applied force.

## VII. Discussion

Motility assays show that microtubules driven by molecular motors can exhibit straight, circular (at locked-curvature) and oscillatory motions.<sup>7,11,12</sup> Inspired by these observations, we proposed the simplest model of a motor-driven filament with free-ends using an applied ‘follower-force’ of constant magnitude. The point force  $f_p$  can be applied anywhere along the filament, not necessarily at the two ends. When  $f_p$  is applied at the proximal end, the filament exhibits a Hopf bifurcation, and transitions from a stable straight configuration to decaying then sustained oscillations, reminiscent of the Hopf bifurcation reported in ref. 31 and 32 for a clamped filament. When  $f_p$  is applied at the distal end, the filament’s straight configuration is unconditionally stable. In between, the portion of the filament ahead of the force location experiences compressive stress while the trailing portion is under tension. This interplay of compressive and tensile stresses along the filament gives rise to a novel instability, as the force magnitude increases beyond a threshold value, where the filament buckles into a configuration with locked curvature and undergoes circular motion in the plane, analogous to

experimentally observed trajectories of microtubules driven by motor proteins.<sup>7</sup> A simple scaling argument shows that the length scale that is relevant for the transition to the locked curvature is not the length of the full filament, but of the portion that is under compression.

Motivated by these findings, we proposed a yet simpler spring-bead model. The results of this model support our findings in the filament model that the trailing portion that is under tension plays an important role in these morphological transitions. Taken together, the results from the filament and spring-bead model suggest that neither structural nor actuation asymmetries in motor-driven microtubules are needed to produce buckled states at locked curvature.

The filament model proposed here is an ideal representation of a motor-driven microtubule. In the real system, molecular motors bind and unbind stochastically to microtubules. Further, in the motility assays that motivated this study, the molecular motors are fixed to the substrate and do not move with the microtubules, but other motors get in contact with the microtubules as they are transported by the action of bound motors. Despite the limitations of the current model, we use it to roughly gauge whether the morphological transitions reported in this study are biologically-relevant to the mechanics of motor-driven microtubules. The force exerted on microtubules by the molecular motors is known to be of the order of pico-Newton ( $\approx 1\text{--}10 \text{ pN}$ ) and microtubules are approximately  $20 \mu\text{m}$  in length. Assuming, following,<sup>31</sup> that the bending rigidity  $A \approx 10 \text{ pN } \mu\text{m}^2$ , we get that for the transition observed at the largest dimensionless force value  $FL^3/A = 300$ , the dimensional force density  $f_p = 300(10)/20^3 = 3/8 \text{ pN } \mu\text{m}^{-1}$ . Thus, the force value must be about  $7.5 \text{ pN}$ , which is within what is biologically achievable by a single molecular motor.

A few comments relating our findings to recent studies on active microfilaments are in order. In particular, a spiraling instability reminiscent of the buckling instability with locked configuration is observed in untethered flexible chains subject to uniform and non-uniform tangential forces.<sup>14,15,17,40</sup> The spiraling

mode seems to depend on the structural (polymer-like) model of the chain, which is fundamentally distinct from the filament model considered here, and the presence of thermal fluctuations. Our model is based on a continuum rod theory and it is closest to the models considered in ref. 31 and 32.

The work in this study is a first step towards developing more realistic mechanics-based models of the full interplay of molecular motors with microtubules. Future extension of this work will account for the stochastic binding of molecular motors. In ongoing work, we are extending this model to account for long range hydrodynamic effects of the viscous fluid using slender body theory.<sup>41</sup> We are particularly interested in the interaction of multiple filaments connected kinematically (*via* structural elements) and dynamically (*via* molecular motors) to model the internal axoneme structure of cilia and flagella.<sup>32,42–44</sup> These models will provide the basis to address complex systems in cellular biophysics, from the mechanisms underlying self-sustained oscillations in flagellar mechanics to flow transport by ciliary beds.

## Conflicts of interest

There are no conflicts to declare.

## References

- B. Alberts, D. Bray and J. Lewis, *Molecular biology of the cell*, Garland Science, New York, NY, 6th edn, 2008.
- S. Etienne-Manneville, *Annu. Rev. Cell Dev. Biol.*, 2013, **29**, 471.
- M. J. Shelley, *Annu. Rev. Fluid Mech.*, 2016, **48**, 487.
- F. Gittes, B. Mickey, J. Nettleton and J. Howard, *J. Cell Biol.*, 1993, **120**, 923.
- F. Gittes, E. Meyhofer, S. Baek and J. Howard, *Biophys. J.*, 1996, **70**, 418.
- J. Howard, A. J. Hudspeth and R. D. Vale, *Nature*, 1989, **342**, 154.
- L. Liu, E. Tuzel and J. L. Ross, *J. Phys.: Condens. Matter*, 2011, **23**, 374104.
- Y. Sumino, K. H. Nagai, Y. Shitaka, D. Tanaka, K. Yoshikawa, H. Chate and K. Oiwa, *Nature*, 2012, **483**, 448.
- L. Bourdieu, T. Duke, M. B. Elowitz, D. A. Winkelmann, S. Leibler and A. Libchaber, *Phys. Rev. Lett.*, 1995, **75**, 176.
- K. Sekimoto, N. Mori, K. Tawada and Y. Toyoshima, *Phys. Rev. Lett.*, 1995, **75**, 172.
- A. M. R. Kabir and A. Kakugo, *Polym. J.*, 2018, **50**, 1139.
- F. Ziebert, H. Mohrbach and I. M. Kulić, *Phys. Rev. Lett.*, 2015, **114**, 148101.
- S. P. Pearce, M. Heil, O. E. Jensen, G. W. Jones and A. Prokop, *ArXiv*, 2018.
- R. E. Isele-Holder, J. Jäger, G. Saggiorato, J. Elgeti and G. Gompper, *Soft Matter*, 2015, **12**, 8451.
- R. E. Isele-Holder, J. Elgeti and G. Gompper, *Soft Matter*, 2016, **11**, 7181.
- D. Sarkar and S. Thakur, *J. Chem. Phys.*, 2017, **146**, 154901.
- S. K. Anand and S. P. Singh, *Phys. Rev. E*, 2018, **98**, 042501.
- P. V. Bayly and K. S. Wilson, *J. R. Soc., Interface*, 2015, **12**, 20150124.
- C. H. Wiggins and R. E. Goldstein, *Phys. Rev. Lett.*, 1998, **20**, 3879.
- C. H. Wiggins, D. Riveline, A. Ott and R. E. Goldstein, *Biophys. J.*, 1998, **74**, 1043.
- R. E. Goldstein, T. R. Powers and C. H. Wiggins, *Phys. Rev. Lett.*, 1998, **80**, 5232.
- Y. Man, K. Lyndon and E. Lauga, *EPL*, 2016, **116**, 24002.
- Y. Man, W. Page, R. J. Poole and E. Lauga, *Phys. Rev. Fluids*, 2017, **2**, 123101.
- T. Gao, R. Blackwell, M. A. Glaser, M. D. Betterton and M. J. Shelley, *Phys. Rev. Lett.*, 2015, **114**, 048101.
- L. E. Becker and M. J. Shelley, *Phys. Rev. Lett.*, 2001, **87**, 198301.
- P. Gosselina, H. Mohrbachbc, I. M. Kulić and F. Ziebert, *Phys. D*, 2016, **318–319**, 105.
- K. R. Prathyusha, S. Henkes and R. Sknepnek, *Phys. Rev. E*, 2018, **97**, 022606.
- O. Duman, R. E. Isele-Holder, J. Elgeti and G. Gompper, *Soft Matter*, 2018, **14**, 4483.
- T. R. Powers, *Rev. Mod. Phys.*, 2010, **82**, 1607.
- R. G. Winkler, J. Elgeti and G. Gompper, *J. Phys. Soc. Jpn.*, 2017, **86**, 101014.
- G. D. Canio, E. Lauga and R. E. Goldstein, *J. R. Soc., Interface*, 2017, **14**, 20170491.
- F. Ling, H. Guo and E. Kanso, *J. R. Soc., Interface*, 2018, **15**, 20180594.
- Y.-N. Young, *Phys. Rev. E: Stat., Nonlinear, Soft Matter Phys.*, 2010, **82**, 016309.
- Y. Liu, B. Chakrabarti, D. Saintillan, A. Lindner and O. du Roure, *Proc. Natl. Acad. Sci. U. S. A.*, 2018, **38**, 9438.
- Y.-N. Young and M. J. Shelley, *Phys. Rev. Lett.*, 2007, **99**, 058303.
- C. W. Wolgemuth, T. R. Powers and R. E. Goldstein, *Phys. Rev. Lett.*, 2000, **84**, 1623.
- R. G. Cox, *J. Fluid Mech.*, 1970, **44**, 791.
- E. Lauga and T. R. Powers, *Rep. Prog. Phys.*, 2009, **72**, 096601.
- See ESI† for numerical method details.
- Y.-K. Wang, C.-J. Lo and W.-C. Lo, *Phys. Rev. E*, 2018, **98**, 062613.
- A. K. Tornberg and M. J. Shelley, *J. Comput. Phys.*, 2004, **196**, 8–40.
- P. V. Bayly and S. K. Dutcher, *J. R. Soc., Interface*, 2016, **13**, 20160523.
- T. Hu and P. V. Bayly, *Cytoskeleton*, 2018, **75**, 185.
- P. Sartori, V. F. Geyer, A. Scholich, F. Jülicher and J. Howard, *eLife*, 2016, **5**, e13258.